Rare Metal Materials and Engineering
Volume 52, Issue 7, July 2023
Available online at www.rmme.ac.cn

Science Press

Cite this article as: Li Yong, Yan Jijun, Fu Rong, et al. Interfacial Behavior, Electronic Properties, and Micromechanics Properties of $L1_2$-Al_3Zr/Al Alloy[J]. Rare Metal Materials and Engineering, 2023, 52(07): 2404-2414.

ARTICLE

Interfacial Behavior, Electronic Properties, and Micromechanics Properties of $L1_2$-Al_3Zr/Al Alloy

Li Yong[1,3,4], Yan Jijun[1,3,4], Fu Rong[2,3,4], Zhang Xieyi[1,3,4], Huang Yuanchun[1,2,3,4]

[1] Light Alloy Research Institute, Central South University, Changsha 410083, China; [2] College of Mechanical and Electrical Engineering, Central South University, Changsha 410083, China; [3] State Key Laboratory of High Performance Complex Manufacturing, Central South University, Changsha 410083, China; [4] Nonferrous Metal Advanced Structural Materials and Manufacturing Collaborative Innovation Center, Central South University, Changsha 410083, China

Abstract: First-principles simulations were conducted to investigate the micromechanics, thermodynamic, and electrical characteristics of $L1_2$-Al_3Zr/Al alloy. The computional results show that the interface with bulk-like atomic organization possesses excellent adhesion and the highest interface strength. During the machining process, the interface system preferentially fails at the Al side. According to the non-relaxation tensile test results, the $L1_2$-Al_3Zr(001)/Al(001) interface system has the highest tensile stress (16.78 GPa). However, after the relaxation tensile test, the $L1_2$-Al_3Zr(110)/Al(110) interface system has the highest tensile stress (10.18 GPa). Additionally, covalent and metallic bonds are generated between the atoms at interface based on the differential charge density and electronic localized function. The formants of interfacial atom orbitals show that the Al and Zr interface atoms have s-p-d or s-p hybridized orbitals.

Key words: mechanical properties; electronic properties; aluminum alloy; plasticity; intermetallic compound

Due to their outstanding thermal and electrical conductivity, high strength, optimum corrosion resistance, high-temperature resistance, and low density, aluminum alloys are frequently used in the aerospace and transportation industries[1–4]. In some harsh circumstances, the aluminum alloys with even better performance are required. Alloying with transition elements (Sc, Hf, V, Ti, Er) is an effective method to improve the strength, high-temperature resistance, toughness, and oxidation resistance of aluminum alloys, and it can also create the tri-aluminide compounds[5–11]. The strength and toughness of aluminum alloys can be effectively enhanced by adding a small amount of scandium. However, Sc is prohibitively expensive[12–14], which requires low-cost substitute. Therefore, it is found that the tiny addition of inexpensive Zr element can result in the similar enhancement effect[15–17].

The trace addition of Zr element can effectively ameliorate the chemical and physical characteristics of Al-based alloys, resulting in the exceptional thermal and oxidation resistance[18–19]. The intermetallic compounds of $D0_{22}$, $D0_{23}$, and $L1_2$ structures can be formed through the proper addition of Zr into aluminum alloys. Although Al_3Zr of $L1_2$ structure is metastable, it can significantly improve the hardness and strength of Al-based alloys[20–22]. The precipitated Al_3Zr of $L1_2$ structure in Al matrix can increase the creep resistance due to the grain coarsening, and the produced Al_3Zr/Al interface effectively suppresses the dynamic recrystallization[23–24]. The electrical and micromechanics characteristics of advantageous interfaces should be investigated to design the innovative alloys with good toughness and strength. Because the alloys inevitably contain various elements, different phases can be precipitated with different interfaces. Therefore, it is practically impossible to analyze the characteristics of all Al_3Zr/Al interfaces. Fortunately, through the advancement of computer technology and condensed matter physics, the Al_3Zr/Al interfaces can be investigated from the atomistic perspective by density functional theory (DFT) -based first-principles calculations. In this research, Al_3Zr represents the metastable $L1_2$-Al_3Zr, which has superior performance

Received date: November 17, 2022
Foundation item: National Natural Science Foundation of China (U1837207); Supported by High-Performance Computing Center of Central South University
Corresponding author: Huang Yuanchun, Ph. D., Professor, Light Alloy Research Institute, Central South University, Changsha 410083, P. R. China, E-mail: ychuang@csu.edu.cn

compared to $D0_{22}$-Al_3Zr and $D0_{23}$-Al_3Zr. The $L1_2$-Al_3Zr/Al interface has rarely been studied. Recently, it is found that Al alloys contain a large number of low-index interfaces, such as $L1_2$-Al_3Zr(001)/Al(001) and $L1_2$-Al_3Zr(110)/Al(110)[25–27]. The low-index Al_3Zr/Al interface was studied based on DFT theory to provide detailed information about the characteristics of Al-based alloys.

To investigate the properties of interfaces, the Rice Wang (R-W) model and the first-principles computational tensile test (FPCTT) were applied[28–29]. The R-W model illustrates the influence of structure on interfacial system. When the interface system is stretched to the interface plane at proper angles, FPCTT can reflect the micromechanics characteristics of interface system. Two methods were used to analyze the mechanical and electrical properties based on FPCTT. One of the methods is the stiff method, which has already been applied to analyze the grain boundaries[30–31]. At specific interfaces, introducing a pre-crack is suitable for analysis. The relaxation method is another way to explore the weakest point and characterize the fracture process of interface systems. In this research, based on the interface models established through edge-to-edge theory, the electrical characteristics of the interface system were investigated. The instability of the Rice ratio and stacking fault energy along several slip directions were also studied to describe the low-index interfacial systems.

1 Computational Method

Vienna Ab-initio Simulation Package was employed for analysis[32]. The bulk characteristics of Al_3Zr and Al were investigated through the local-density approximation (LDA), Perdew-Burke-Ernzerh (PBE), and Perdew-Wang-91 (PW91) methods, which could obtain the appropriate potential and simulation approach[33]. The force tolerance and energy tolerance were set as 0.1 eV/nm and 5×10^{-7} eV/atom to achieve the precise total energy and internal stress[34–35], respectively. Finally, considering the asymmetric surfaces of slab models, the dipole correction along z-axis direction was activated, whose distance interval was 1.7 nm[36].

1.1 Properties of Al_3Zr and Al bulk materials

The Al and Al_3Zr bulk materials were optimized by PW91, PBE, and LDA potentials to ensure the calculation accuracy and to determine the formation enthalpy and lattice constants of Al_3Zr and Al materials. The calculated results were then compared with the experimental and calculated values, as shown in Table 1. The enthalpy of Al_3Zr formation (ΔH^f) can be calculated by Eq.(1), as follows:

$$\Delta H^{f} = \frac{1}{4}\left(\mu_{Al_3Zr}^{bulk} - 3\mu_{Al}^{bulk} - \mu_{Zr}^{bulk}\right) \quad (1)$$

where μ_{Al}^{bulk}, $\mu_{Al_3Zr}^{bulk}$, and μ_{Zr}^{bulk} are total energies corresponding to Al, Al_3Zr, and Zr, respectively.

According to Table 1, it can be seen that the overall calculation results by LDA and PBE methods agree well with the experiment results. However, the formation enthalpy is underestimated by LDA method. Although the formation enthalpy calculated by PW91 method agrees well with the experiment results, the lattice constant (0.397 nm) is significantly overestimated. Hence, PBE method was chosen for analysis in this research.

The elastic constants of three potentials (C_{11}, C_{12}, and C_{44}) were also calculated to ensure the structural stability, and the results are shown in Table 2. The elastic constants can satisfy the generalized stability requirements for cubic crystals: $C_{11}+2C_{12}>0$, $C_{11}>|C_{12}|$, and $C_{44}>0$. The Young's modulus (E), Poisson ratio (v), and Bulk modulus (B) were calculated by the Voigt-Reuss-Hill method. The results in Table 2 are consistent well with the experiment results. Therefore, the employed calculation method is reasonable, and the optimized structure is stable.

1.2 Characteristics of low-index surfaces

The accurate surface energy, interface energy, and adhesion work were obtained through a correct slab model with enough thickness. The (001), (110), and (111) surface models for Al_3Zr and Al bulk materials were established with different numbers of layers to achieve the proper thickness of models. To obtain a reasonable surface model, the optimized models with different layer distances (Δ_{ij}, %) were applied, and the deviation of layer distance of slab models can be calculated by Eq.(2), as follows:

$$\Delta_{ij} = \frac{d_{ij}^{sur} - d_{be}^{sur}}{d_{be}^{sur}} \times 100\% \quad (2)$$

where d_{ij}^{sur} is the plane spacing of the optimized surface model with $j=i+1$; d_{be}^{sur} refers to the layer spacing of un-optimized models from optimized Al or Al_3Zr bulk materials. The calculation results of layer distances are shown in Table 3.

As for (001) and (110) surface models, $|\Delta_{45}|$ is less than 2%, as shown in Table 3. Hence, the 9-atom layers are sufficient to present the bulk-like interior of these two surfaces. Since $|\Delta_{34}|$ is less than 2% for (111) surface, the 7-atom layers are sufficiently thick.

1.3 Interface modeling

The edge-to-edge theory was used to connect the surface models, and the most typical low-index interfaces were

Table 1 Calculated and experimental lattice constant (a) and formation enthalpy (ΔH^f) of Al_3Zr and Al bulk materials by PW91, PBE, and LDA methods

Material	Parameter	LDA	PW91	PBE	Experiment result	Ref.
Al_3Zr	Lattice constant, a/nm	0.405	0.397	0.409	[0.403, 0.412]	[37–38]
	Formation enthalpy, ΔH^f/kJ·mol^{-1}	−43.59	−44.37	−44.54	[−44.07, −44.75]	[39]
Al	Lattice constant, a/nm	0.404	0.402	0.403	[0.397, 0.405]	[37–38]
	Formation enthalpy, ΔH^f/kJ·mol^{-1}	0	0	0	0	[38]

Table 2 Bulk modulus (*B*), elastic constant, Poisson ratio (*v*), and Young's modulus (*E*) of Al_3Zr and Al bulk materials

Material	Method	C_{11}/GPa	C_{44}/GPa	C_{12}/GPa	*E*/GPa	*B*/GPa	*v*	Ref.
Al	LDA	112.7	32.3	56.9	80.6	75.5	0.322	-
	PW91	115.6	33.7	59.2	83.0	78.0	0.323	-
	PBE	116.9	33.4	58.4	83.7	77.9	0.321	-
	Experiment	109–125.8	31.6–37.9	53.7–64.5	78.9–91.9	75.8–79.3	0.317–0.320	[39]
Al_3Zr	LDA	182.1	75.9	63.2	168.8	102.8	0.226	-
	PW91	181.7	79.2	62.9	172.2	102.5	0.219	-
	PBE	182.3	77.4	64.1	170.3	103.5	0.226	-
	Experiment	179.3–189.3	62.7–84.4	59.2–66.1	153.2–181.3	102.0–107.2	0.218–0.242	[39]

Table 3 Deviation results of layer distance of different slab models after optimization (%)

Material	Deviation, Δ_{ij}	(001) surface			(110) surface			(111) surface		
		5 layers	7 layers	9 layers	5 layers	7 layers	9 layers	5 layers	7 layers	9 layers
Al_3Zr-AlZr	Δ_{12}	−11.9	8.2	10.2	6.4	5.7	11.9	−10.4	8.6	−7.2
	Δ_{23}	7.1	5.3	4.7	8.1	3.3	8.7	6.8	4.5	5.3
	Δ_{34}	-	−3.7	−2.8	-	2.7	−1.6	-	−0.8	1.9
	Δ_{45}	-	-	−1.2	-	-	0.9	-	-	0.4
Al_3Zr -Al	Δ_{12}	8.7	6.0	11.2	12.4	−8.7	9.9	-	-	-
	Δ_{23}	−3.3	4.3	6.5	7.6	6.3	−5.2	-	-	-
	Δ_{34}	-	−1.5	1.9	-	2.7	3.8	-	-	-
	Δ_{45}	-	-	1.9	-	-	−1.4	-	-	-
Al	Δ_{12}	9.2	7.7	6.5	8.9	11.3	6.7	4.5	5.7	10.2
	Δ_{23}	2.5	4.3	3.1	4.2	2.7	4.4	2.2	3.6	8.5
	Δ_{34}	-	1.2	1.7	-	2.2	1.6	-	1.4	1.7
	Δ_{45}	-	-	0.9	-	-	0.6	-	-	1.1

established with various atomic stacking configurations. To prevent the interaction between two neighboring free surfaces, the $Al_3Zr(001)$/Al(001), $Al_3Zr(110)$/Al(110), and $Al_3Zr(111)$/Al(111) interfacial models were established with distance interval of 1.5 nm at each termination. Fig. 1 shows the schematic diagrams of interface models, where blue lines denote the interface; Al and Zr atoms are represented by white and black balls, respectively; Al atoms of Al matrix side are represented by red balls. The interfacial atomic stacking patterns are also shown in Fig. 1, and the dotted rectangular areas show the stacking modes of Al side.

After optimization, the mismatch of the low-index $Al_3Zr(001)$ /Al(001), $Al_3Zr(110)$/Al(110), and $Al_3Zr(111)$/Al(111) interface models was 3.46%, 2.97%, and 2.21%, respectively. These mismatches were all below 5%, indicating that the lattice distortion was minimal and the structure was stable.

2 Results and Discussion

2.1 Surface energy

For the Al slab model, the surface energy γ_{sur} can be obtained by Eq.(3), as follows:

$$\gamma_{sur} = \frac{E_{Al}^{slab} - N_{Al}\mu_{Al}^{bulk}}{2A} \quad (3)$$

where N represents the number of atoms; μ_{Al}^{bulk} is the energy of one Al atom in the bulk material; E_{Al}^{slab} denotes the total energy of Al surface model; A represents the single surface area; the subscript indicates the element or compound related to the parameters.

Eq. (4) can be used to calculate the total energy of Al_3Zr surface system, as follows:

$$\gamma_{sur} = \frac{1}{2A}\left(E_{slab} - N_{Al}\mu_{Al}^{slab} - N_{Zr}\mu_{Zr}^{slab}\right) \quad (4)$$

where μ_i^{slab} refers to the energy of an individual i atom in bulk materials; E_{slab} donates the total energy of interface system.

Because $Al_3Zr(111)$ surface is stoichiometric, the γ_{sur} value can be obtained by Eq.(5), as follows:

$$\gamma_{sur} = \frac{1}{2A}\left(E_{slab} - N_{Zr}\mu_{Al_3Zr}^{bulk}\right) \quad (5)$$

However, for the $Al_3Zr(001)$ and $Al_3Zr(110)$ surfaces, the surfaces of symmetric slab models are non-stoichiometric. Then, Eq.(6) can be obtained from Eq.(4), based on the results in Ref.[35,37], as follows:

$$\gamma_{sur}=\frac{1}{2A}\left\{E_{slab}-N_{Zr}\mu_{Al_3Zr}^{bulk}+(3N_{Zr}-N_{Al})\left[\mu_{Al}^{bulk}+(\mu_{Al}^{slab}-\mu_{Al}^{bulk})\right]\right\} \quad (6)$$

The chemical potential of the stoichiometric surface of Al_3Zr should be equal to that of Al_3Zr bulk material. Additionally, the chemical potentials of Al slab atom and Zr slab atom are less than those of Al bulk atom and Zr bulk atom, respectively. Thus, Eq. (7) and Eq. (8) can be obtained, as follows:

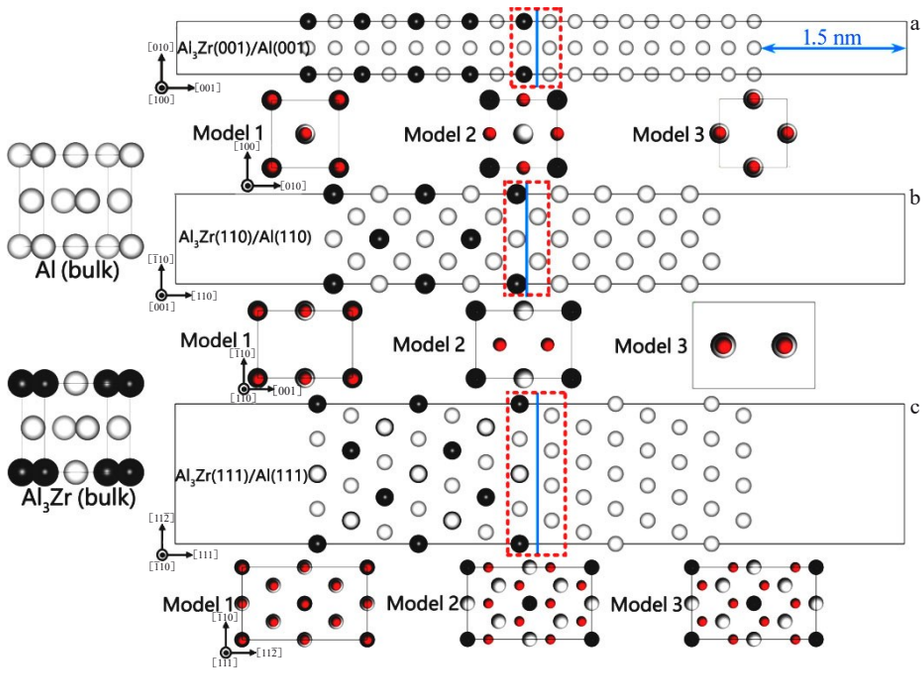

Fig.1 Schematic diagrams of atomic arrangement and interface system of $Al_3Zr(001)/Al(001)$ interface (a), $Al_3Zr(110)/Al(110)$ interface (b), and $Al_3Zr(111)/Al(111)$ interface (c)

$$\begin{cases} 3\mu_{\mathrm{Al}}^{\mathrm{bulk}} + \mu_{\mathrm{Zr}}^{\mathrm{bulk}} + \Delta H^{\mathrm{f}} = \mu_{\mathrm{Al_3Zr}}^{\mathrm{bulk}} \\ 3\mu_{\mathrm{Al}}^{\mathrm{slab}} + \mu_{\mathrm{Zr}}^{\mathrm{slab}} = \mu_{\mathrm{Al_3Zr}}^{\mathrm{bulk}} \end{cases} \tag{7}$$

$$\begin{cases} \mu_{\mathrm{Al}}^{\mathrm{slab}} - \mu_{\mathrm{Al}}^{\mathrm{bulk}} < 0 \\ \mu_{\mathrm{Zr}}^{\mathrm{bulk}} - \mu_{\mathrm{Zr}}^{\mathrm{slab}} > 0 \end{cases} \tag{8}$$

Combining Eq.(7) with Eq.(8), Eq.(9) can be obtained, as follows:

$$\frac{1}{3}\Delta H^{\mathrm{f}} < \mu_{\mathrm{Al}}^{\mathrm{slab}} - \mu_{\mathrm{Al}}^{\mathrm{bulk}} < 0 \tag{9}$$

Subsequently, the surface energy of Al and Al_3Zr is shown in Fig. 2. The surface energies of $Al_3Zr(111)$ and Al surface systems are constant. However, when the chemical environment changes, the surface energies of $Al_3Zr(001)$ and $Al_3Zr(110)$ surface systems change. When $\mu_{\mathrm{Al}}^{\mathrm{slab}} - \mu_{\mathrm{Al}}^{\mathrm{bulk}}$ increases, the surface energy of Al_3Zr/Al interface decreases, whereas that of $Al_3Zr/AlZr$ interface increases.

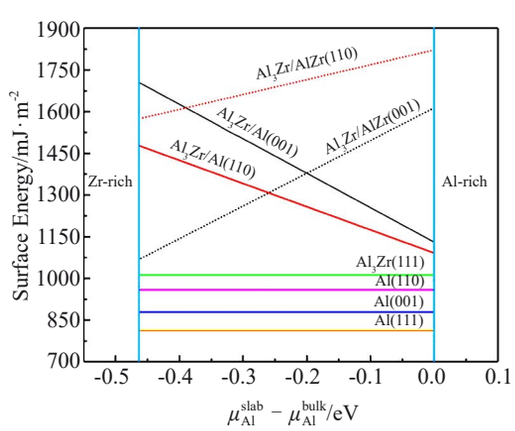

Fig.2 Surface energies of Al and Al_3Zr surface systems

2.2 Electronic and micromechanical characteristics

2.2.1 Theoretical tensile stress and separation energy of Al_3Zr/Al system

The stiff method was selected to examine the strength and wettability of Al_3Zr/Al interface, therefore determining the interfacial characteristics. Then, the electronic structures and bonding features of the strongest interfaces were investigated. The interface system was separated at the pre-crack plane (the blue lines in Fig.1) with sampling distance of 0.03 nm at each step in the stiff method. Since every atom had a fixed position, the system was separated at the target interface. Then, the interfacial strength and separation energy were estimated through the relationship between separation energy and separation distance.

The separation energy (E_{sep}) can be acquired by Eq.(10), as follows:

$$E_{\mathrm{sep}} = \frac{E_{\mathrm{st}} - E_{\mathrm{init}}}{A} \tag{10}$$

where E_{st} and E_{init} represent the optimized system energy with and without separation, respectively. The relationship between E_{sep} and separation distance x can be obtained by Eq.(11)[38], follows:

$$f(x) = E_{\mathrm{sep}} - E_{\mathrm{sep}}\left(1 + \frac{x}{\lambda}\right)\mathrm{e}^{-\frac{x}{\lambda}} \tag{11}$$

where λ is the eigenvalue of the Thomas-Fermi screening length. Eq.(11) can be used to characterize the interactions between atoms. The optimal relationship between atom distance and stress is constructed after conversion (differentiating $f(x)$), particularly in metal materials. Eq.(12) yields the tensile stress, as follows:

$$f'(x) = \frac{E_{\mathrm{sep}}x}{\lambda^2}\mathrm{e}^{-\frac{x}{\lambda}} \tag{12}$$

The maximum theoretical tensile stress (σ_{max}) occurs when $x=\lambda$, and σ_{max} is defined by Eq.(13), as follows:

$$\sigma_{max}=f'(x)=\frac{E_{sep}x}{\lambda^2}e^{-\frac{x}{\lambda}}=\frac{E_{sep}}{\lambda e} \quad (13)$$

Generally, the adhesion work (W_{ad}) reflects the wettability, which is equal to the maximal separation energy. The theoretical tensile stress and separation energy produced by the stiff method can be calculated, and the results are shown in Fig.3 and Table 4. Model 2 has the maximum adhesion work, namely optimal wettability (Fig.3), and the highest theoretical tensile stress. These models have identical characteristics, i.e., the alignment rule of coherent interfaces and the atoms is similar to that of Al_3Zr or Al bulk materials. This phenomenon suggests that the interfacial strength of the low-index interface is largely influenced by the interface structure.

According to Fig. 3, only Model 2 has greater adhesion work than Al, whereas Model 1 and Model 3 have significantly lower adhesion work, indicating that these two systems are more brittle at the interface. The optimal wettability (W_{ad}=2.82 J/m^2) is achieved for Al_3Zr(110)/Al(110) interface, namely Model 2. Model 1 and Model 3 have similar strengthening effects for Al_3Zr(111)/Al(111) interface, and Model 2 has the most obvious strengthening effect. The tensile stress of bulk material of Model 2 is 11.82 GPa, which is higher than that of pure Al by 47%. According to Fig.3 and Table 4, for the low-index interfaces, the strengthening degree of Model 2 is more than 30%, whereas Model 1 and Model 3 have relatively weak strengthening degree on the interface. The better adhesion and greater strength ensure the enhancement of nucleation, fine-tuning grains, and strengthening effects.

Because Model 2 has the strongest interface with the best wettability, each index interface of Model 2 was discussed. To predict the fracture behavior of interface systems, the relaxation method was used to analyze the interface performance during processing. The surface energy is determined, as shown in Table 4. Then, the interface energy γ_{int} was calculated by Eq.(14), as follows:

$$\gamma_{int}=\frac{1}{A}\{E_{int}-N_{Zr}\mu^{bulk}_{Al_3Zr}+(3N_{Zr}-N_{Al,1})[\mu^{bulk}_{Al}+(\mu^{slab}_{Al}-\mu^{bulk}_{Al})]-N_{Al,2}\mu^{bulk}_{Al}\}-\gamma_{s,Al(hkl)}-\gamma_{s,Al_3Zr(hkl)} \quad (14)$$

where $N_{Al,1}$ and $N_{Al,2}$ represent the number of Al atoms on the side of Al_3Zr and Al, respectively; $\mu^{slab}_{Al}-\mu^{bulk}_{Al}$ and $\mu^{slab}_{Al}-\mu^{bulk}_{Al}$ refer to the surface energy of Al(*hkl*) and Al_3Zr/Al(*hkl*), respectively; E_{int} is the total energy of interface system; $\gamma_{s,Al(hkl)}$ and $\gamma_{s,Al_3Zr(hkl)}$ represent the surface energy of the Al(*hkl*) and Al_3Zr(*hkl*), respectively.

According to Fig.4, the interface energy is decreased with increasing the $\mu^{slab}_{Al}-\mu^{bulk}_{Al}$ value. According to Fig. 1, the interface is located in an Al-rich environment. Consequently, $\mu^{slab}_{Al}-\mu^{bulk}_{Al}$ value approaches to zero and the γ_{sur} values for Al_3Zr(001)/Al(001), Al_3Zr(110)/Al(110), and Al_3Zr(111)/Al(111) interfaces are 1613.6, 1822.4, and 1012.3 mJ/m^2, respectively.

Then, the interface energies of (001), (110), and (111) surfaces are obtained as 138, 49, and 57 mJ/m^2, respectively, which indicates the thermodynamic stability of these interfaces.

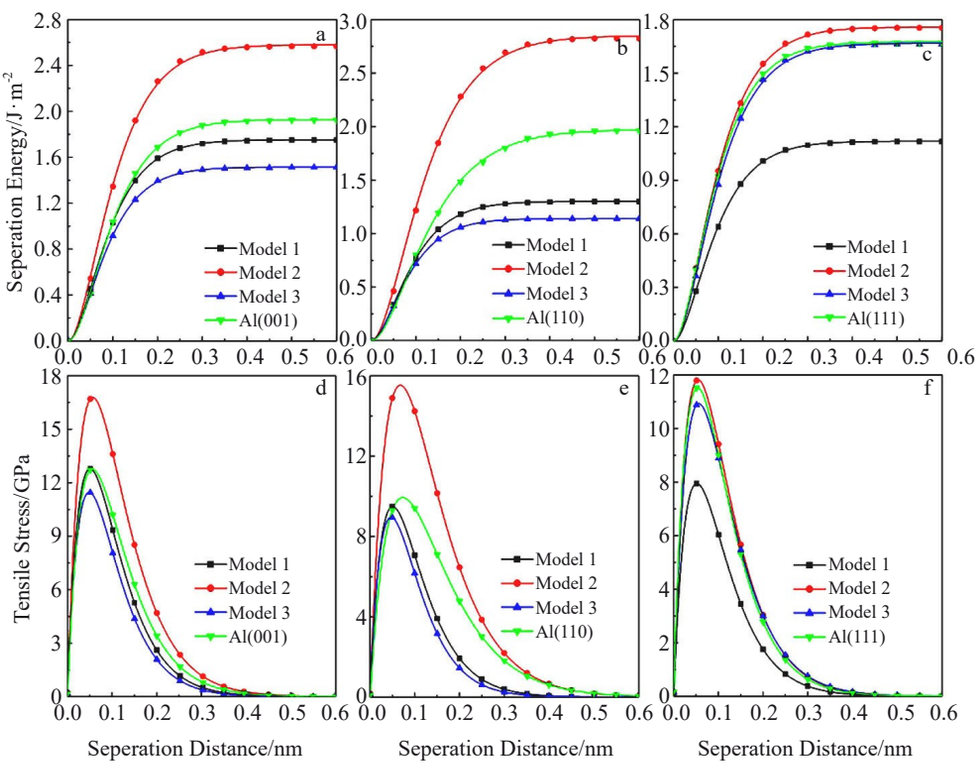

Fig.3 Separation energy (a–c) and theoretical tensile stress (d–f) of Al_3Zr(001)/Al(001) interface (a, d), Al_3Zr(110)/Al(110) interface (b, e), and Al_3Zr(111)/Al(111) interface (c, f) through stiff method

Table 4 Surface energy γ_{sur} of Al_3Zr/Al and Al bulk materials and interface energy γ_{int} of Model 2

Orientation	Interface distance, d_0/nm	$\gamma_{sur}(Al_3Zr/Al)$/mJ·m^{-2}	$\gamma_{int}(Al_3Zr/Al)$/mJ·m^{-2}	$\gamma_{sur}(Al)$/mJ·m^{-2}
(001)	0.2105	1069.8–1613.6	136.2–680.2	138
(110)	0.1391	1574.0–1822.4	49.4–357.4	49
(111)	0.2329	1012.3	59.2	57

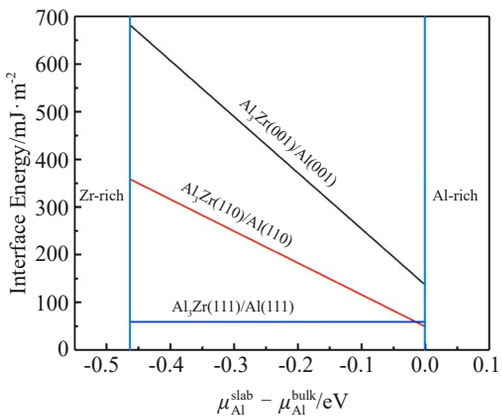

Fig.4 Interface energies of different Al_3Zr/Al interface systems

To further investigate the interface strength, the differential charge density was also estimated (Fig. 5) to provide more information of the charge and bonding characteristics of the interfaces. The related electronic localized functions (ELF) of the red dotted lines in Fig. 5 are presented. The blue area in Fig. 5 reflects the decrease in electronic cloud, whereas the yellow area indicates the increase in electronic cloud. The electrons of Al and Zr atoms move to the space between two phases, where the electrons are collected and the new chemical bonds are also generated to strengthen the interface. The electrons gathered at $Al_3Zr(001)/Al(001)$ interface on the Al phase are near the Al_3Zr phase of $Al_3Zr(110)/Al(110)$ interface system. The electron cloud of $Al_3Zr(111)/Al(111)$ interface system is evenly dispersed at the interface, as shown in Fig. 5f, where the red area denotes the localized electrons and the blue area denotes the electron gas. It is evident that the largest electronic-localized degree of $Al_3Zr(001)/Al(001)$, $Al_3Zr(110)/Al(110)$, and $Al_3Zr(111)/Al(111)$ interfaces is 0.701, 0.705, and 0.703, respectively. The proportion of red area in Fig.5d and 5e is much larger than that in Fig.5f, which indicates that the atoms in $Al_3Zr(001)/Al(001)$ and $Al_3Zr(110)/Al(110)$ interfaces provide a larger number of covalent bonds than $Al_3Zr(111)/Al(111)$ interface does because of the higher interface strength of the former two interfaces. The order of the interface energy is as follows: $Al_3Zr(110)/Al(110)$>$Al_3Zr(001)/Al(001)$>$Al_3Zr(111)/Al(111)$.

2.2.2 Electronic structure, bonding characteristics, and fracture behavior of interface systems

During the machining process, the fracture does not occur

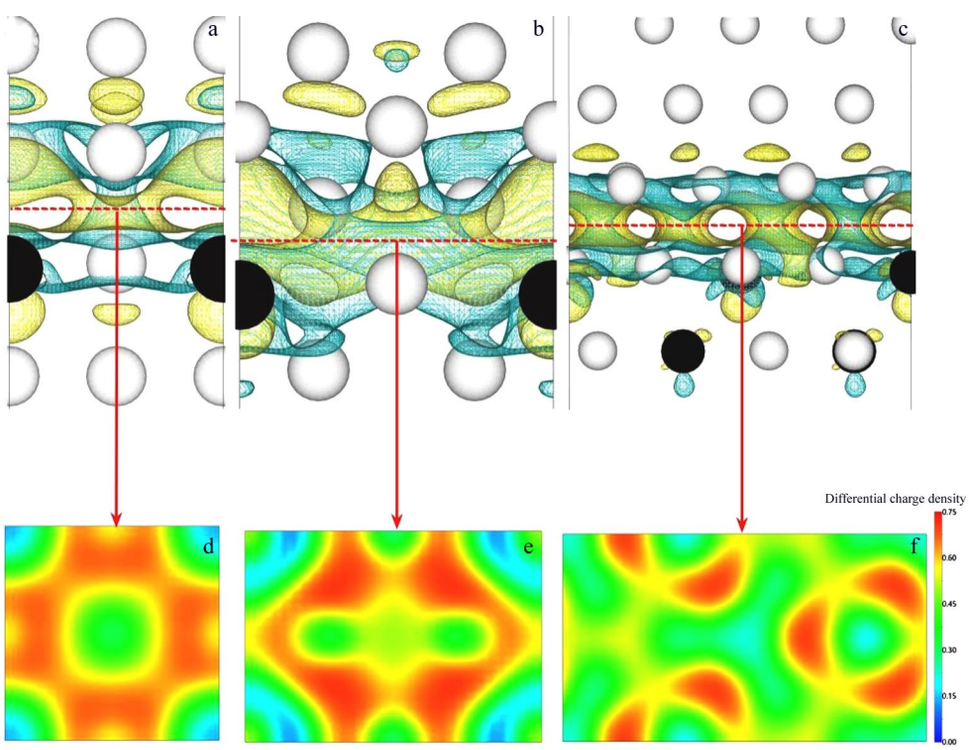

Fig.5 ELFs (a–c) and differential charge density (d–f) of $Al_3Zr(001)/Al(001)$ interface (a, d), $Al_3Zr(110)/Al(110)$ interface (b, e), and $Al_3Zr(111)/Al(111)$ interface (c, f) of Model 2 interface system

at the interface but at the weakest position. Therefore, the Al_3Zr(001)/Al(001), Al_3Zr(110)/Al(110), and Al_3Zr(111)/Al(111) interfaces were investigated through the relaxation method to discuss the fracture behavior and tensile strength of interface systems. The interface system is stretched perpendicularly to the interface during the relaxation. Only the terminal atoms are fixed in the computation, so the system breaks at the weakest point. The weakest position can be identified during the stretching process, and the related theoretical tensile stress can be calculated precisely. Fig. 6 shows the separation energy and tensile stress with different separation distances. For Al_3Zr(001)/Al(001) and Al_3Zr(110)/Al(110) interfaces, the variation in separation energy has two stages. The interface system collapses at the weakest location because of the increase in separation energy at the critical point, and then it instantly falls to a constant value. As for Al_3Zr(111)/Al(111) surface, the variation of separation energy has three stages. The separation energy dramatically increases at the initial stage, and then the increasing rate is abruptly decreased at separation distance of 0.31 nm. Then, the separation energy decreases to a constant value. As shown in Fig. 6, the Al_3Zr(001)/Al(001) interface has the longest fracture distance (0.481 nm). Besides, the maximum tensile stress of 10.18 GPa is obtained for the Al_3Zr(110)/Al(110) interface system after relaxation, whereas that before relaxation is 16.78 GPa for the Al_3Zr(001)/Al(001) interface system.

It is concluded that the Al_3Zr(110)/Al(110) interface system improves the interfacial strength. Work of adhesion and the maximum tensile stress of different interface systems are listed in Table 5.

Although the theoretical tensile stress illustrates the strength of interface system, the fracture process should be thoroughly discussed based on the deep mechanism. Therefore, the electronic structure and fracture process of Al_3Zr(001)/Al(001) interface system are shown in Fig. 7. Two layers of Al atoms are adsorbed at the Al_3Zr side. According to Fig. 7f–7h, the electron cloud density barely changes with the stretching proceeding. Besides, the electron reduction areas can be observed in Fig. 7i. Finally, the system cracks at the Al side.

Fig. 8 illustrates the electronic structure and fracture behavior of Al_3Zr(110)/Al(110) interface system in stretching process. It can be seen that the interface system fractures at the Al side during the stretching and the Al atoms of two layers are bonded to the Al_3Zr side, forming a deep fracture surface with double atomic layer of V-shape, as shown in Fig. 8a–8e. Fig. 8f–8j present the variation of electronic cloud density during the stretching process. The electronic cloud changes noticeably from Fig. 8f to Fig. 8h. The electronic cloud at various points on the Al side shrinks, as indicated by the red dotted circles in Fig. 8i. Then, the atomic vacuum is generated due to the formation of electronic cloud holes, therefore forming the fracture surface. Finally, the electronic vacuum region occurs as the interface system fails.

Fig. 9 describes the electronic structure and fracture behavior of Al_3Zr(111)/Al(111) interface system. The distinct rearrangement of atoms in this interface system (Fig. 9c–9d) fits well with the abrupt decrease in the tensile stress of Al_3Zr(111)/Al(111) interface system (Fig. 6b). Finally, one Al atomic layer is adsorbed as a flat plane on the Al_3Zr side, and the fracture surface is visible on the Al side. The change in electronic cloud is not obvious in Fig. 9f and 9g. After that, two electronic vacuum zones are formed due to the continuous stretching process and the obvious atom rearrangement. As seen in Fig. 9j, the two vacuum regions are finally linked, indicating that the interface system fractures along this electronic vacuum area.

2.2.3 Partial density of states and bonding characteristic

The partial density of states (PDOS) of bulk materials and Al_3Zr(001)/Al(001) interface system is shown in Fig. 10. The energy range of PDOS>0 in Fig. 10d–10f is narrower than that in Fig. 10a–10c. As shown in Fig. 10d–10f, PDOS disappears when the exergy (E) exceeds 2.71 eV, suggesting the interfacial energy reduction. It can also be seen that new formants of Al and Zr appear at energy of −1.94 eV after the interface formation, suggesting that new s-p-d or s-p hybrid orbitals are generated and new chemical bonds are formed. These results fit well with those from Fig. 5. Additionally, it is

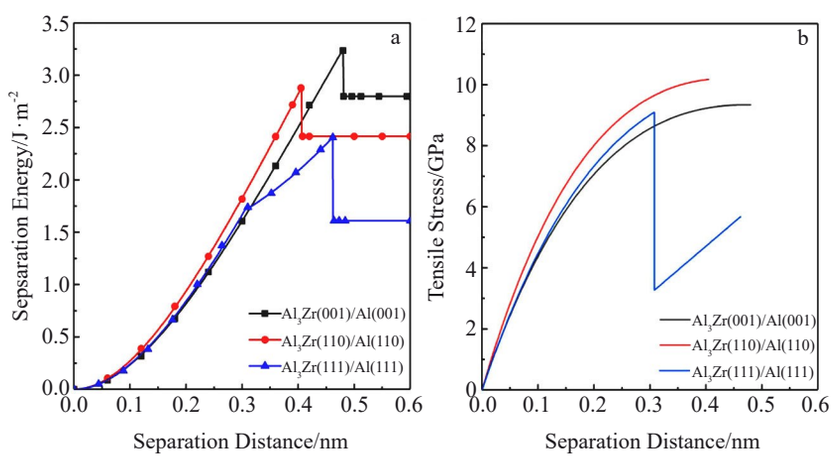

Fig.6 Separation energy (a) and tensile stress (b) of different interface systems by relaxation method

Table 5 Work of adhesion (W_{ad}) and maximum tensile stress (σ_{max}) of different interfaces

Method	Interface	W_{ad}/J·m^{-2}	σ_{max}/GPa
Stiff	(001)	2.57	16.78
	(110)	2.82	15.52
	(111)	1.75	11.82
Relaxed	(001)	3.24	9.34
	(110)	2.87	10.18
	(111)	2.41	9.10

found that PDOS is not zero at the Fermi level (E_f), indicating that several energy bands exist and the metallic bonding is formed.

Fig. 11 shows PDOS of bulk materials and Al_3Zr(110)/Al(110) interface system. It can be seen that PDOS vanishes when E>2.83 eV. When the energy is −0.92, 2.11, and 3.01 eV, new formants of Al, AlZr-Al, and Zr occur, respectively, as shown in Fig.11d–11f, thereby producing new chemical bonds and s-p-d hybrid orbitals. Additionally, PDOS is not 0 at E_f=0 in the Al_3Zr(110)/Al(110) interface system, indicating that this

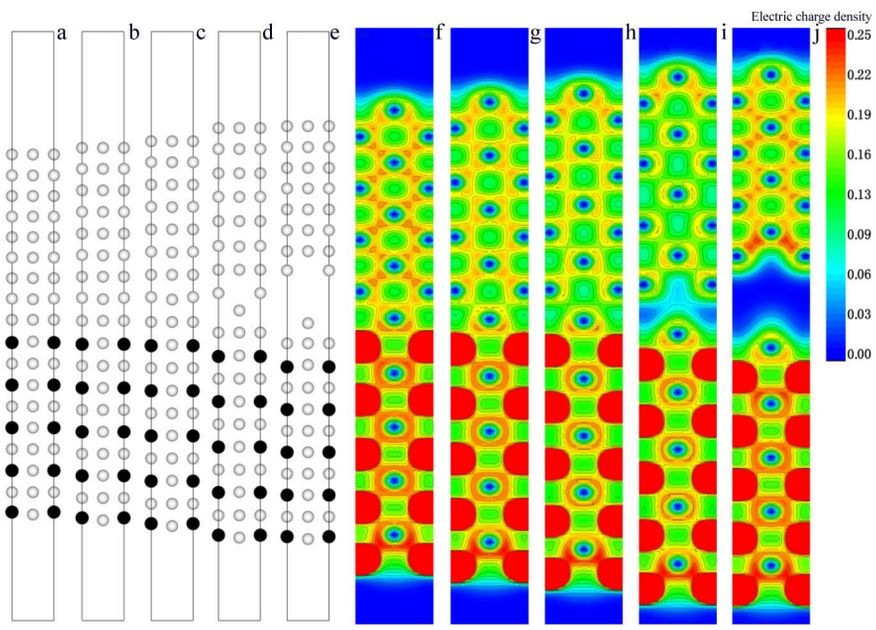

Fig.7 Atomic structures (a–e) and corresponding electronic structures (f–j) of Al_3Zr(001)/Al(001) interface system in stretching process

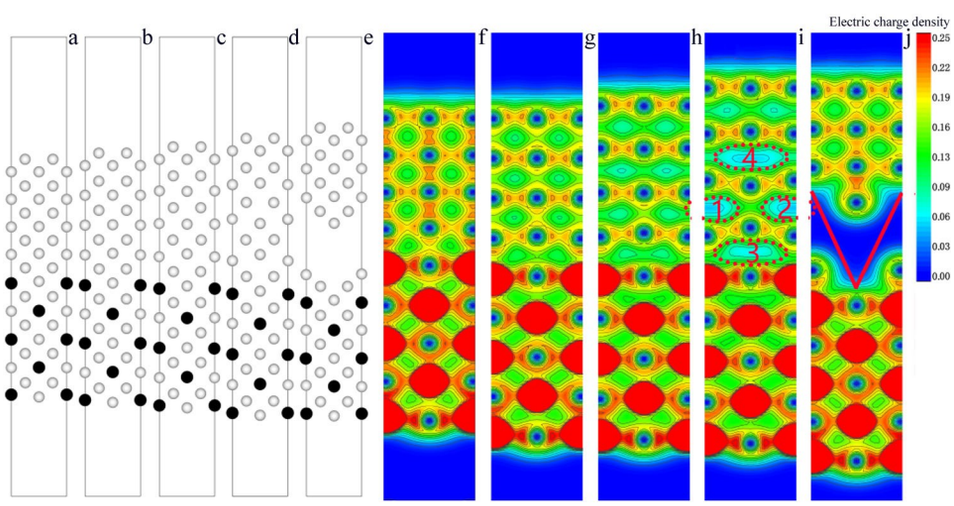

Fig.8 Atomic structures (a–e) and corresponding electronic structures (f–j) of Al_3Zr(110)/Al(110) interface system in stretching process

system is a conductor and numerous energy bands exist at the Fermi level.

According to Fig. 12d–12f, the energy range narrows when the energy is below 2.41 eV. Moreover, the new formants of Al, AlZr-Al, and Zr appear at E=−2.28 and 1.55 eV, suggesting that the new s-p-d hybrid orbitals and chemical bonds are generated.

2.2.4 Plasticity and stacking fault energy of interface

Rice ratio (D) and stacking fault energy (γ_{GSF}) were used to demonstrate the interface plasticity[40–41] in this research. The interfacial system is subjected to force for deformation, which induces dislocations for the interfacial slip or causes

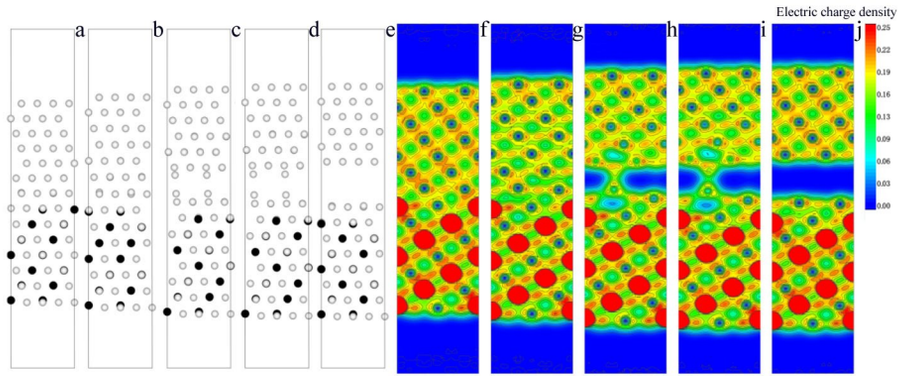

Fig.9 Atomic structures (a–e) and corresponding electronic structures (f–j) of $Al_3Zr(111)/Al(111)$ interface system in stretching process

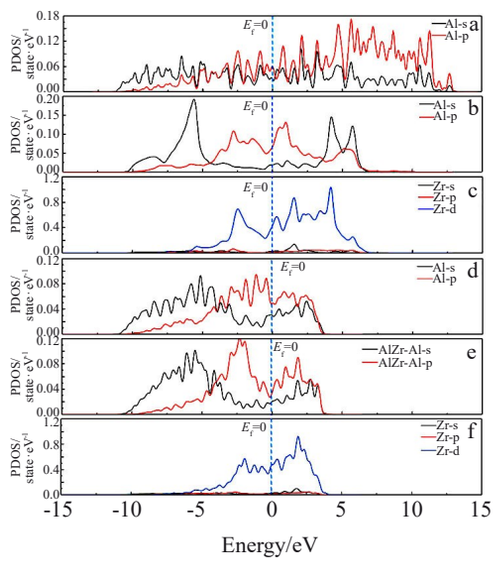

Fig.10 PDOS of Al bulk material (a), Al (b) and Zr (c) spectra of Al_3Zr bulk material, and Al (d), AlZr-Al (e), and Zr (f) spectra of $Al_3Zr(001)/Al(001)$ interface system

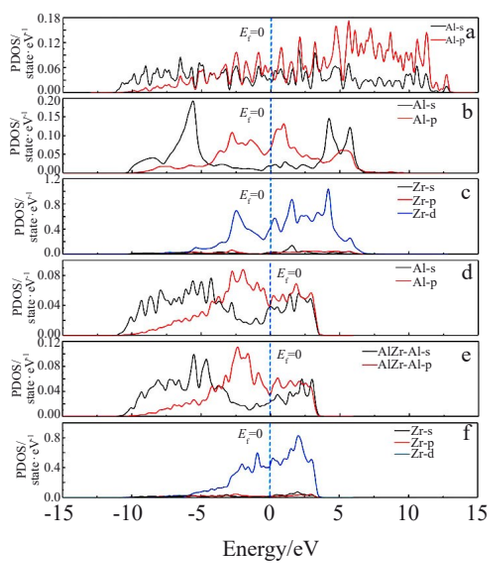

Fig.11 PDOS of Al bulk material (a), Al (b) and Zr (c) spectra of Al_3Zr bulk material, and Al (d), AlZr-Al (e), and Zr (f) spectra of $Al_3Zr(110)/Al(110)$ interface system

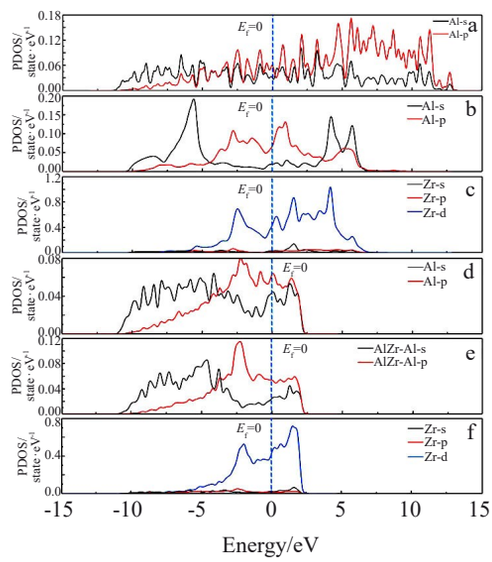

Fig.12 PDOS of Al bulk material (a), Al (b) and Zr (c) spectra of Al_3Zr bulk material, and Al (d), AlZr-Al (e), and Zr (f) spectra of $Al_3Zr(111)/Al(111)$ interface system

interfacial cleavage. Generally, G_c is the initiation energy for interface crack, and the dislocation appears at the interface when the critical energy $(G_d) \leqslant W_{ad}$. There is a relationship between the maximum stacking fault energy (γ_{us}) and the critical energy (G_d) [42–43]. Two blocks must cross the generalized stacking fault when they produce relative slippage. γ_{GSF} can be calculated by Eq.(15), as follows:

$$\gamma_{GSF} = \frac{E_{init} - E_{sf}}{A} \tag{15}$$

where E_{sf} represents the entire energy corresponding to the system with stacking defect, and E_{init} indicates the total energy corresponding to the interface system optimized without any stacking defect. In this case, γ_{us} stands for maximum γ_{GSF}. Then, Rice ratio can be used to determine the plasticity of interface system, as follows:

$$D = \frac{G_c}{G_d} = \frac{W_{ad}}{\gamma_{us}} \tag{16}$$

It is concluded that if D<1, the interface system is brittle; if D>1, the interface system is plastic.

Fig. 13 depicts the generalized stacking fault energy, and

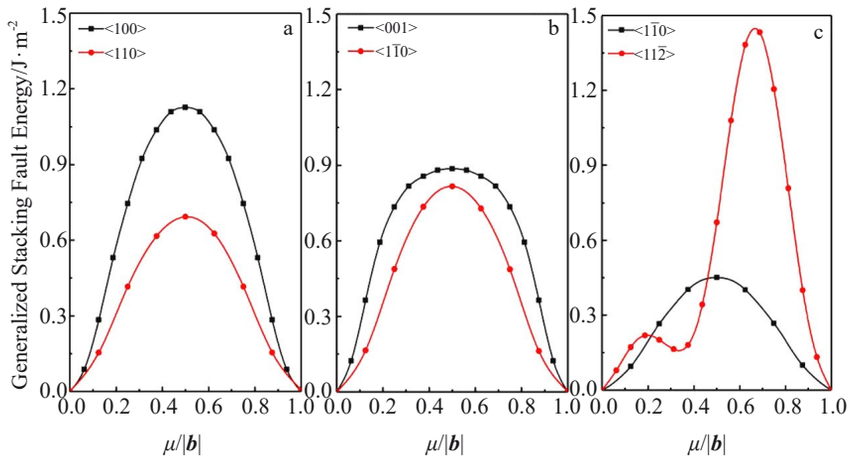

Fig.13 Generalized stacking fault energies of Al_3Zr(001)/Al(001) (a), Al_3Zr(110)/Al(110) (b), and Al_3Zr(111)/Al(111) (c) interface systems along different slip directions

Table 6 Maximum generalized unstable stacking fault energy (γ_{us}) and representative Rice ratio (D) of Al_3Zr(001)/Al(001), Al_3Zr(110)/Al(110), and Al_3Zr(111)/Al(111) interface systems

Interface system	Al_3Zr (001)/Al(001)		Al_3 Zr (110)/Al(110)		Al_3Zr(111)/Al(111)	
	<100>	<110>	<001>	<$\bar{1}$10>	<$\bar{1}$10>	<11$\bar{2}$>
γ_{us}/J·m^{-2}	1.13	0.69	0.88	0.82	0.45	0.22/1.45
D	2.29	3.72	3.20	3.44	3.89	7.95/1.21

Table 6 shows γ_{us} and D values of different interfacial systems to reflect their plasticity. It can be seen that the D values are in the range of 2.29–3.72 when the Al_3Zr(001)/Al(001) interface slip occurs along <001> and <110> directions, and the corresponding γ_{us} is 1.13 and 0.69 J/m^2, respectively. This result indicates that the Al_3Zr(001)/Al(001) interface has good flexibility along <001> and <110> directions. The γ_{us} of Al_3Zr(110)/Al(110) interface along <001> and <$\bar{1}$10> directions is 0.88 and 0.82 J/m^2, and the corresponding D is 3.02 and 3.44, respectively. Al_3Zr(110)/Al(110) interface slip easily occurs along <$\bar{1}$10> direction. According to Fig. 13c, it can be inferred that the Al_3Zr(111)/Al(111) interface (γ_{us}=0.22 J/m^2, D=7.95) can easily slip along <11$\bar{2}$> direction. The best plasticity can be obtained for the Al_3Zr(111)/Al(111) interface along <11$\bar{2}$> direction. However, when $\mu/|\boldsymbol{b}|$ (the ratio of slip distance to the value of Burgers vector) exceeds 0.182, γ_{us}= 1.45 J/m^2 and D=1.21, indicating that the system needs much more energy and the preferred slip direction changes to <$\bar{1}$10> direction.

3 Conclusions

1) The interface has a bulk-like atomic arrangement, which results in the greatest interface strength and adhesion work, and the interface is more brittle on the aluminum side. The Al_3Zr(110)/Al(110) interface has the highest tensile stress, whereas the Al_3Zr(001)/Al(001) interface has the highest strength.

2) The metallic bonding and covalent bonding are formed, and the s-p-d and s-p hybrid orbitals are generated at the interfaces.

3) Al_3Zr(001)/Al(001), Al_3Zr(110)/Al(110), and Al_3Zr(111)/Al(111) interfaces have strong plasticity along specific directions. The best plasticity can be obtained for the Al_3Zr(111)/Al(111) interface along <11$\bar{2}$> direction.

References

1 Yan F, Zhang K, Yang B Y *et al*. *Optics & Laser Technology*[J], 2021, 138: 106 843

2 Wang L, Liu Y, Yang C G *et al*. *Journal of Materials Processing Technology*[J], 2021, 292: 117 053

3 Muhammad M, Nezhadfar P D, Thompson S *et al*. *International Journal of Fatigue*[J], 2021, 146: 106 165

4 Wu W L, Song Y L, Zhou P *et al*. *Journal of Alloys and Compounds*[J], 2021, 861: 157 987

5 Yan K, Chen Z W, Zhao Y N *et al*. *Journal of Alloys and Compounds*[J], 2021, 861: 158 491

6 Khomutov M, Chereshneva A, Petrovskiy P *et al*. *Journal of Alloys and Compounds*[J], 2021, 858: 157 644

7 Kong Y P, Jia Z L, Liu Z P *et al*. *Journal of Alloys and Compounds*[J], 2021, 857: 157 611

8 Liu Y, Wen J C, Zhang X Y *et al*. *Physical Chemistry Chemical Physics*[J], 2021, 23(8): 4718

9 Xue H T, Luo Y Q, Tang F L *et al*. *Materials Chemistry and Physics*[J], 2021, 258: 123 977

10 Dumbre J, Kairy S K, Anber E *et al*. *Journal of Alloys and Compounds*[J], 2021, 861: 158 511

11 Avtokratova E, Sitdikov O, Markushev M *et al*. *Materials Science and Engineering A*[J], 2021, 806: 140 818

12 Mochugovskiy A G, Mikhaylovskaya A V, Tabachkova N Y *et al*. *Materials Science and Engineering A*[J], 2019, 744: 195

13 Vo N Q, Dunand D C, Seidman D N. *Acta Materialia*[J], 2014, 63: 73
14 Yang D X, Li X Y, He D Y *et al*. *Materials Science and Engineering A*[J], 2013, 561: 226
15 Wang Z H, Lin X, Tang Y *et al*. *Journal of Materials Science & Technology*[J], 2021, 69: 168
16 Jiang L, Rouxel B, Langan T *et al*. *Acta Materialia*[J], 2021, 206: 116 634
17 Tian S K, Li J Y, Zhang J L *et al*. *Journal of Materials Research and Technology*[J], 2019, 8(5): 4130
18 Xu C, Xiao W L, Zheng R X *et al*. *Materials & Design*[J], 2015, 88: 485
19 Orlova T S, Latynina T A, Murashkin M Y *et al*. *Journal of Alloys and Compounds*[J], 2021, 859: 157 775
20 Kumar N, Mishra R S. *Materials Science and Engineering A*[J], 2013, 580: 175
21 Ren Z X, Qin J Q, Liu R P *et al*. *Journal of Alloys and Compounds*[J], 2020, 825: 153 825
22 Yang T X, Wei M Z, Ding Z Y *et al*. *Calphad*[J], 2020, 69: 101 768
23 Farkoosh A R, Dunand D C, Seidman D N. *Journal of Alloys and Compounds*[J], 2020, 820: 153 383
24 Gubicza J, El-Tahawy M, Lábár J L *et al*. *Journal of Materials Science*[J], 2020, 55: 16 791
25 Saha S, Todorova T Z, Zwanziger J W. *Acta Materialia*[J], 2015, 89: 109 115
26 Qiu C H, Su Y S, Zhang D *et al*. *Metallurgical and Materials Transactions A*[J], 2021, 53(4): 1308
27 Li H, Xu P Y, Lu S B *et al*. *Rare Metal Materials and Engineering*[J], 2020, 49(6): 1873
28 Peng W J, Peng H, Wu G X *et al*. *Computational Materials Science*[J], 2020, 171: 109 204
29 Li J H, Zhao X, Wang D S *et al*. *Acta Metallurgica Sinica* (*English Letters*)[J], 2013, 26(6): 675
30 Zhou H B, Zhang Y, Liu Y L *et al*. *Journal of Physics: Condensed Matter*[J], 2009, 21(17): 175 407
31 Zhang Y, Lu G H, Wang T *et al*. *Materials Transactions*[J], 2006, 47(11): 2678
32 Gorbunova M A, Shein I R, Makurin Y N *et al*. *Physica B: Condensed Matter*[J], 2007, 400(1–2): 47
33 Song W, Wang B, Wang J L *et al*. *Journal of Cluster Science*[J], 2017, 28(5): 2575
34 Deák P, Aradi B, Frauenheim T *et al*. *Physical Review B*[J], 2010, 81: 153 203
35 Zhang J Y, Dang W Q, Ao Z M *et al*. *Physical Chemistry Chemical Physics*[J], 2015, 17: 8994
36 Bengtsson L. *Physical Review B*[J], 1999, 59(19): 12 301
37 Li S S, Li L, Han J *et al*. *Applied Surface Science*[J], 2020, 526: 146 455
38 Yang T X, Wei M Z, Ding Z Y *et al*. *Calphad*[J], 2020, 69: 101 768
39 Clouet E, Nastar M, Sigli C. *Physical Review B*[J], 2004, 69(6): 64 109
40 Sun S P, Li X P, Wang H J *et al*. *Applied Surface Science*[J], 2014, 288: 609
41 Rose J H, Ferrante J, Smith J R. *Physical Review Letters*[J], 1981, 47(9): 675
42 Rice J R, Thomson R. *The Philosophical Magazine*[J], 1974, 29(1): 73
43 Rice J R. *Journal of the Mechanics and Physics of Solids*[J], 1992, 40(2): 239

$L1_2$-Al_3Zr/Al合金的界面行为、电子性质和微观力学性质

黎　勇[1,3,4]，严积珺[1,3,4]，付　绒[2,3,4]，张燮义[1,3,4]，黄元春[1,2,3,4]
(1. 中南大学 轻合金研究院，湖南 长沙 410083)
(2. 中南大学 机电工程学院，湖南 长沙 410083)
(3. 中南大学 高性能复杂制造国家重点实验室，湖南 长沙 410083)
(4. 中南大学 有色金属先进结构材料与制造协同创新中心，湖南 长沙 410083)

摘　要：使用第一性原理模拟研究$L1_2$-Al_3Zr/Al合金的微力学、热力学和电学特性。计算结果显示，具有类体材料原子堆叠方式的界面具有最好的粘附性和最高的界面强度。在加工过程中，界面系统更倾向于在Al一侧发生解离。非驰豫拉伸测试结果表明，$L1_2$-Al_3Zr(001)/Al(001)界面系统表现出最高的拉伸应力（16.78 GPa），而对于驰豫拉伸，$L1_2$-Al_3Zr(110)/Al(110)界面系统的拉伸应力最高（10.18 GPa）。此外，电子云密度和电子局域化函数表明界面上的原子形成了共价键和金属键。界面原子轨道的共振峰表明，界面Al和Zr原子产生了s-p-d或s-p杂化轨道。

关键词：力学性能；电子性质；铝合金；塑性；金属间化合物

作者简介：黎　勇，男，1968年生，博士，高级工程师，中南大学轻合金研究院，湖南 长沙 410083，E-mail：1640851658@qq.com